Highlights

Online Detection and Identification of Cathode Cracking in Lithiumion Battery Cells

Shanthan K. Padisala, Sara Sattarzadeh, Satadru Dey

- Real-time cathode crack detection and estimation.
- Coupled single particle and crack degradation models.
- Cascaded filter-based algorithmic framework.

Online Detection and Identification of Cathode Cracking in Lithium-ion Battery Cells

Shanthan K. Padisala^{1,*}, Sara Sattarzadeh¹, Satadru Dev¹

Abstract

Cyclic charging and discharging of Lithium-ion (Li-ion) battery cells lead to the contraction and expansion of the battery electrodes. These contractions and expansions result in the development of internal stresses within the electrodes, further culminating in the growth of cracks. Typically, the cracks in anodes lead to an increase in the surface area hence facilitating a faster SEI layer growth, and a lot of research to model such faults has already been conducted in this area. However, when it comes to cracks in the cathode, the research is still a little under-explored. Not detecting the potential cathode crack growth may lead to quick degradation of battery cells which results in capacity fade or resistance growth. If these kinds of faulty batteries are not detected, it may result in hazardous scenarios like battery fires even during nominal usage. Therefore, the real-time monitoring of these cathode cracks is essential for health-conscious battery operation. This paper is an attempt to design such real-time monitoring algorithm that can detect and identify crack growths in the cathode. The algorithm is developed by fusing a variation of the Single Particle Model (SPM) capturing Lithium concentration dynamics in the cathode and an empirical model capturing crack growth – in conjunction with real-time feedback-based coupled filters. The coupled filter consists of two filters working in cascade where the first filter generates a primary residual based on cathode SPM and terminal voltage feedback. Subsequently, the second filter utilizes this primary residual as feedback in

^{*}Corresponding author: S. K. Padisala

Email addresses: sfp5587@psu.edu (Shanthan K. Padisala), sfs6216@psu.edu (Sara Sattarzadeh), skd5685@psu.edu (Satadru Dey)

¹S. K. Padisala and S. Dey are with the Department of Mechanical Engineering, The Pennsylvania State University, University Park, PA 16802, USA. During her part of this work, S. Sattarzadeh was with The Pennsylvania State University.

conjunction with the empirical crack growth model – ultimately producing an estimate of the crack growth. This estimated crack growth is used to detect and identify the cathode cracking mechanism. Proposed approach is tested with experimental as well as simulation studies, illustrating its effectiveness.

Keywords:

Batteries, Cathode Cracking, Mechanical Failure, Battery Faults, Observers, Detection, and Identification.

1. Introduction

There are numerous reasons why batteries degrade over time. These reasons could be any of the following few listed - chemical reactions within the battery cell due to the charging and discharging, impact of operating conditions like temperature and environment, the inherent shelf-life of the battery cells, internal damages that arise due to manufacturing defects, and external damages that may occur by abusive conditions. This degradation can potentially manifest themselves as abnormal Solid Electrolyte Interface (SEI) layer growth, Lithium plating, mechanical degradation inside the electrode, loss of Lithium inventory or active material [1]. This work focuses on a specific type of mechanical degradation, namely, cathode cracking [2] – and develops a real-time monitoring algorithm that can detect and identify cathode crack growths.

Various efforts have been made to model crack propagation and growth in battery electrodes – ranging from physics principle based models to simplified empirical models. The works [3], [4] and [5] describe the process of crack propagation as a result of the stresses induced due to repeated cell charge/discharge. [6] investigates the degradation mechanisms of high-capacity 18650 lithium-ion batteries with Si-graphite anode and nickel-rich NMC cathode. In [7], a comprehensive review of mechanical degradation models have been performed while connecting them to the electrochemical battery models. In [8], Barai et al. modelled the effect of crack growth to a more fundamental quantity – changes in the effective diffusion constant, which ultimately is used to model the reduction in the cell capacity. In [9], a single particle battery model with chemical/mechanical degradation physics has been proposed for the purposes of battery health estimation. Along similar lines, Dong et al. proposed a physics-based aging model with coupled chemical/mechanical degradation mechanisms, which essentially shows the

effect of crack growth in cell capacity fade [10].

Another line of research is focused on the experimental investigation of cathode cracking in battery cells. For example, the work [11] focuses on the experimental validation of the cracks that are developed due to over-charging of the battery cells in the cathodes. The experimental validation was performed using the images collected from the advanced scanning transmission electron microscope, which resulted in a conclusion that a high cutoff voltage cycling induced intragranular cracking in the cathode. Xu et al. designed cycling tests to investigate the influence of voltage window and C-rate on electrode degradation[12].

In addition to these mentioned research findings, it was found that Zhang et al. discuss the challenges and progress in designing cathodes [13]. Lim et al. explored the intrinsic origins of crack generation in cathode materials for Li-ion batteries [14]. Bland et al. in their work discussed the chemical and electrochemical conditions present within stress corrosion and corrosion fatigue cracks, which are major causes of material failure [15]. In a similar line of research, Xu et al. have conducted an experimental investigation of the mechanical and structural degradation of (Nickel Manganese Cobalt) NMC cathodes [16].

Although the aforementioned works shed light on the cathode crack mechanisms through modeling, analysis, and experimental investigations, there has been a lack of research in real-time monitoring of such cathode cracks. Particularly, models can be practically limited due to one or more of the following factors: computational complexity and lack of adaptability in realworld scenarios. In this context, simplified model-based estimators that utilize real-time feedback can be useful in monitoring cathode cracks. Along this line, an electrochemical model-based observer was designed in [17] where the effects of intercalation-induced stresses on electrode diffusion were considered. This work estimates Lithium concentration as well as the radial and tangential stresses within the electrode. There are a few key differences between [17] and our current work. First, [17] focuses mainly on anode stresses. Second, the algorithm in [17] estimates the electrode stresses, however, it does not extend these estimates to actual crack information in the electrode. Such crack information can be crucial in predicting the battery life – depending on when the crack area reaches its maximum allowable limit. Hence, there exist a gap in literature where real-time monitoring of cathode crack mechanism remains under-explored. In our current work, we consider the cracks in cathode and utilizes a crack model to directly estimate the crack area which

in turn can be used for battery life prediction.

Based on the aforementioned discussion, the main contribution of this work can be summarized as follows: We propose a model-based scheme for detection and identification of cathode cracks in real-time. We utilize a combination of electrochemical model (namely, Single Particle Model (SPM) [18]), a crack model affecting the cathode diffusion coefficient [8], and a set of diagnostic filters to develop the algorithmic framework. It consists of two filters working in cascade. The first filter, denoted as the primary residual filter, utilizes SPM cathode model and terminal voltage feedback to generate a primary residual signal. This primary residual signal is essentially the difference between the estimates from a closed-loop filter and an open-loop filter – where both filters use SPM cathode, however, one with voltage feedback (closed-loop) and the other without feedback (open-loop). The second filter, denoted as the crack estimation filter, utilizes this primary residual signal as feedback along with a crack propagation model [8] to estimate the cathode crack area in real-time.

Next, we clarify the novelty of this work in relation to some of the previous works from our group where electrode-level estimation/diagnostics were performed using cascaded observer/filter-based schemes. The works [19, 20] proposed electrode-level charge and health estimation techniques, however, they utilized phenomenological integrator-type simplified electrode models and did not consider specific cathode crack phenomenon in their formulation. The work in [21] performs voltage and thermal fault detection under electrochemical and thermal anomalies, but it does not specifically focus on cathode crack detection and estimation. The conference paper [22] developed some preliminary ideas used in this current work, especially the use of the difference between closed-loop and open-loop estimates as electrode-level residual signals. This current work extends our preliminary conference work [22] by: (i) specifically focusing on cathode cracking, instead of generic electrode-level faults considered in [22], (ii) further elaborating on the mathematical convergence analysis of the algorithm, and (iii) performing experimental studies to illustrate the effectiveness of the proposed algorithm.

The rest of the paper is organized as follows: Section 2 discusses the modeling of the Cathode Cracking Mechanism. Section 3 discusses the crack detection and identification algorithm developed by us for this problem and finally, the results and conclusions are discussed in detail in section 4.

2. Battery Model

We discuss the nominal cathode dynamical model followed by the cracking dynamics.

2.1. Modeling of nominal cathode operation

The first step in the modeling process is to capture the nominal cathode dynamics which generally involves charge and discharge. Here, we adopt Single Particle Modeling (SPM) framework which captures the charge/discharge process in terms of Lithium concentration within the electrodes [18, 23]. Essentially, SPM leads to two parabolic Partial Differential Equations (PDEs) involves diffusion of lithium ions in cathode and anode. From this SPM framework, we utilize the cathode diffusion PDE, as given below:

$$\frac{\partial C^{+}}{\partial t} = \frac{D_{s}^{+}}{r^{2}} \frac{\partial}{\partial r} \left(r^{2} \frac{\partial C^{+}}{\partial r} \right), \tag{1}$$

$$\frac{\partial C^{+}}{\partial t} = \frac{D_{s}^{+}}{r^{2}} \frac{\partial}{\partial r} \left(r^{2} \frac{\partial C^{+}}{\partial r} \right), \qquad (1)$$

$$\frac{\partial C^{+}}{\partial r}|_{r=0} = 0; \frac{\partial C^{+}}{\partial r}|_{r=R^{+}} = \frac{+I}{a_{s}^{+} F D_{s}^{+} A^{+} L^{+}}, \qquad (2)$$

where the superscript + indicates the positive electrode, Lithium concentration $[mol/m^3]$ in electrodes is C, Input current A is represented by I, the specific surface area $[m^2/m^3]$ is represented by a_s , F is Faraday's constant, effective diffusion coefficient in solid phase $[m^2/s]$ is represented by D_s , the radius of the particle [m] is represented by R, the area of the current collector $\lfloor m^2 \rfloor$ is represented by A and finally, the length of the electrode $\lfloor m \rfloor$ is represented by L. In addition, the positive current represents the current from the battery (discharging) and the negative current represents the current into the battery (charging).

Next, the SPM framework models the terminal voltage of the battery by mapping the Lithium concentrations of anode and cathode into the open circuit potentials – along with a few other terms arising from Butler-Volmer kinetics and film resistances [18]. However, such open circuit potentials (OCPs) maps are difficult to obtain in practice, as the exact material properties of anode and cathode materials may not be always known. To overcome this limitation, we use two sequential transformations to capture the open circuit behavior. First, we map the cathode surface concentration $C^+|_{r=R^+}$ to anode surface concentration leveraging conservation of Lithium [24]. Then, we map the anode surface concentration to state-of-charge (SOC). Next, we use the open circuit voltage OCV-SOC map to capture the open circuit behavior.

Note that OCV-SOC maps are much easier to obtain even for commercial cells, as compared to OCP maps. To this end, the terminal voltage expression now becomes:

$$V = U(C^{+}|_{r=R^{+}}) - IR(C^{+}|_{r=R^{+}}, I), \tag{3}$$

where U(.) is the composite function arising from the composition of cathodeto-anode transformation, anode-to-SOC transformation, and OCV-SOC map. The resistance R is nonlinear function of the current I and surface concentration state $C^+|_{r=R^+}$. This nonlinear resistance expression can be found from the Butler-Volmer kinetics and film resistances [18].

2.2. Modeling of cathode cracking mechanism

After the nominal cathode operation is modeled, the next step is to introduce the dynamics that arise due to the increment in cathode crack, and ultimately couple those dynamics with the nominal cathode model. Here we adopt a crack model from [8], where the crack damage propagation in time is related to the applied current, and such crack further affects the cathode's diffusion coefficient.

The modeling of the crack is given as follows:

$$\frac{\partial A_{cr}}{\partial t} = \beta_4 (A_{max} - A_{cr})|I| \tag{4}$$

$$D_s^+ = D_{s0}^+ \left(1 - \frac{A_{cr}}{A_{max}} \right)^{\beta_5} \tag{5}$$

where A_{cr} is the amount of damage in the cathode (dimensionless [8]), A_{max} is the maximum possible damage to the cathode, D_{s0}^+ is the original diffusion constant in $[m^2/s]$ in the presence of no crack, D_s^+ is effective diffusion coefficient in $[m^2/s]$ in the presence of crack, and β_4 and β_5 are tuning parameters of this model. The value of A_{max} is computed by the relation as follows [8]:

$$A_{max} = -0.5902 + \frac{0.7173 + 0.0027R^{+} + (-0.15/R^{+})}{1 + |(0.0223I_{c}) - (0.2115 + (-0.002)R^{+})|}$$
(6)

where R^+ is the radius cathode particle and I_c is the C-rate (proportional to the current I) at which the battery is being charged/discharged.

2.3. State-space model formulation

In this subsection, we formulate a state-space model for the cathode dynamics. First, we write the state-space version of the crack model (4) as

$$\dot{z} = \beta_4 (A_{max} - z)|I|,\tag{7}$$

where $z = A_{cr}$ and I is the current.

Subsequently, we focus on nominal cathode model (1)-(2). We use finite difference method to discretize the continuum cathode concentration C^+ into finite number of states denoted by the vector $C = \begin{bmatrix} C_1^+ & C_2^+ & \dots & C_N^+ \end{bmatrix}^T$ [25]. Following the finite difference method utilized in [21, 25], we formulate the following state-space model capturing the nominal cathode operation.

$$\dot{C} = h(z)AC + h(z)BI,\tag{8}$$

$$V = f(C, I), (9)$$

where (8) is derived from (1)-(2), and the output equation (9) is derived from (3). The function $h(z) = (1 - \frac{z}{A_{max}})^{\beta_5}$ captures the dependence of diffusion coefficient on the crack area as shown in (5). The function f(.) is given in (3), and as described in [22], the A and B matrices are given by:

$$A = \left(\frac{D_{s0}^{+}}{\Delta^{2}}\right)$$

$$\begin{bmatrix}
-2 & 2 & 0 & \dots & 0 & 0 \\
\frac{1}{2} & -2 & \frac{3}{2} & \dots & 0 & 0 \\
\vdots & \vdots & \vdots & \dots & \vdots & \vdots \\
0 & 0 & 0 & \dots & 1 - \frac{1}{N-1} & -(1 - \frac{1}{N-1})
\end{bmatrix},$$

$$B = -\left(1 + \frac{1}{N-1}\right) \left[0 & 0 & \dots & \left(\frac{D_{s0}^{+}\theta}{\Delta}\right)\right]^{T}$$
(10)

where D_{s0}^+ is the original diffusion constant in the presence of no crack, Δ is the width of the discretized element (radially), and θ is a constant which is given by $\theta_{\pm} = 1/(Fa^+D_s^+A^+L^+)$. In summary, (7) and (8) represent the state dynamics equation while (9) represent the measured output equation.

3. Crack detection and identification algorithm

In this section, we describe the algorithmic framework for detecting and identifying cathode cracks. The dynamical models of cathode concentration

and cathode crack propagation are adopted from existing literature, as discussed in Sections 2.1 and 2.2. In Section 2.3, we formulate a state-space model based on these dynamical models where cathode concentration and crack area are defined as the system states. In Section 3, we have created a filter structure based on the state-space formulation. The filters are a combination of open-loop state-space model and a feedback term which consists of a design parameter called filter gain. These filter gains are designed based on mathematical conditions described later. Finally, these filters are run online to estimate the system states including the crack area. The crack area is a direct indicator of cathode fracture growth. This is how the proposed approach uses filters to track cathode crack propagation.

A schematic of the framework is illustrated in Fig. 1. It consists of two blocks: primary residual filter and crack estimation filter. The primary residual filter utilizes the state-space model (8)-(9)along with terminal voltage feedback to generate a primary residual r. The crack estimation filter uses this residual r as feedback along with the state-space model (7) to generate a crack estimate \hat{z} . A crack is detected when \hat{z} crosses a threshold z_h , and \hat{z} also serves as an estimate to identify the crack area.

In other words, we aim to achieve the following properties: If there is crack, i.e. $z \neq 0$, then r should be non-zero and \hat{z} is a close estimate of z. On the other hand, if there is no crack, i.e. z = 0, then r and \hat{z} should be close to zero.

We have created a cascaded filter structure instead of a more integrated single filter structure. The main reason behind the choice of such cascaded structure is the ease of analysis and design. The analysis is separated into two parts – the first part deals with cathode concentration dynamics and the second part deals with the crack propagation dynamics. The analysis of error and residual convergence has become simpler due to the cascaded and separated structure. Furthermore, for a more integrated filter structure, two filter gains (one for the cathode concentration dynamics and another one for the crack propagation dynamics) would have to be designed using a single design condition due to their interdependencies – which would have led to numerical complications and additional nonlinearities. However, for the cascaded structure, we separated the two filter gain designs into two sequential conditions – leading to a simpler design approach.

The following subsections discuss these two blocks in detail.

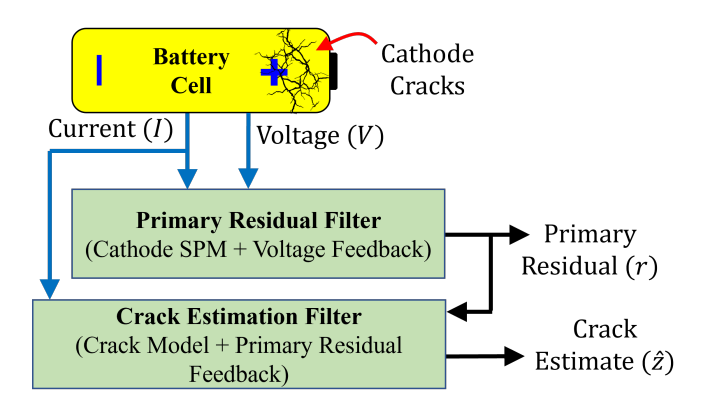


Figure 1: Cathode Cracking detection and identification schematic.

3.1. Primary residual filter

Primary residual filter consists of two filters. Filter #1 is a closed-loop filter given by:

$$\dot{\hat{C}}_1 = A\hat{C}_1 + BI + L_1(V - \hat{V}),\tag{11}$$

$$\hat{V} = f(\hat{C}_1, I), \tag{12}$$

where \hat{C}_1 is the estimated states by this closed-loop filter and L_1 is the filter gain to be designed. Filter #2 is an open-loop filter given by:

$$\dot{\hat{C}}_2 = A\hat{C}_2 + BI,\tag{13}$$

where \hat{C}_2 is the estimated states by this open-loop filter. The primary residual is defined as $r = \hat{C}_1 - \hat{C}_2$. Typical residual generation techniques, such as model- and observer-based ones, use the difference between an estimate and a sensor-measured signal (of the same physical variable) to compute the residuals. The idea behind the residual is to compute the difference between two signals which represent the same physical variable such that the designed residual is sensitive to anomaly or fault. However, for primary residual generation, the system state is cathode concentration, which is not measured by any sensors in commercial battery systems. In the absence of a measured cathode concentration signal, we needed to create two estimates of the cathode concentration in order to subtract them from each other and subsequently compute the residual which will in turn be sensitive to the anomaly. These two estimates came from an open-loop observer and a closed-loop observer.

This is the motivation behind using the difference between closed-loop and open-loop cathode concentration estimates as primary residual. Next, we will use the following propositions to prove the following: If $z \neq 0$, then r should be non-zero, and $r \approx 0$ when z = 0.

Proposition 1. Define the estimation error between the closed-loop filter estimate and actual state as $e = C - \hat{C}_1$, and consider a linear approximation of the function $f(C_1, I) \approx \alpha_1 C_1 + \alpha_2 I$ where α_1 and α_2 are linearization constants. Then, (i) the dynamics of e is stable, and (ii) the steady-state value of e is a function of e, if e is a function of e, if e is Hurwitz stable e is e in e

Proof. Differentiating e with respect to time, and considering (8), (11), and (12) gives us:

$$\dot{e} = \dot{C} - \dot{\hat{C}}_1 = h(z)AC + h(z)BI - A\hat{C}_1 - BI
- L_1(f(C_1, I) - f(\hat{C}_1, I))
= h(z)Ae + (h(z) - 1)(A\hat{C}_1 + BI)
- L_1(f(C_1, I) - f(\hat{C}_1, I))$$
(14)

Considering a linear approximation of f(.), we can write $f(C_1, I) \approx \alpha_1 C_1 + \alpha_2 I$ where α_1 and α_2 are linearization constants. Under this linearized approximation, (14) becomes:

$$\dot{e} = (h(z)A - L_1\alpha_1)e + (h(z) - 1)(A\hat{C}_1 + BI), \tag{15}$$

Choosing the filter gain L_1 such that $(h(z)A - L_1\alpha_1)$ is Hurwitz stable $\forall z \in [0, A_{max}]$, we can conclude that the dynamics of e given in (15) is stable.

Following the stability of (15) and putting $\dot{e} = 0$, we can find the steady-state expression of e as:

$$e = -(h(z)A - L_1\alpha_1)^{-1}(h(z) - 1)(A\hat{C}_1 + BI), \tag{16}$$

which confirms that the steady-state value of e is a function of z.

Proposition 2. If Proposition 1 is true, then (i) the dynamics of primary residual r is stable, and (ii) the steady-state value of r is a function of z.

Proof. Differentiating e with respect to time, and considering (13), (11), and (12) gives us:

$$\dot{r} = \dot{\hat{C}}_1 - \dot{\hat{C}}_2 = A\hat{C}_1 - BI - A\hat{C}_2 - BI
- L_1(f(C_1, I) - f(\hat{C}_1, I))
= Ar - L_1(f(C_1, I) - f(\hat{C}_1, I))$$
(17)

Again, considering the linear approximation $f(C_1, I) \approx \alpha_1 C_1 + \alpha_2 I$, (17) becomes:

$$\dot{r} = Ar - L_1 \alpha_1 e,\tag{18}$$

Applying the expression of e from (16), we can write (18) as

$$\dot{r} = Ar + L_1 \alpha_1 (h(z)A - L_1 \alpha_1)^{-1} (h(z) - 1) (A\hat{C}_1 + BI). \tag{19}$$

Since A is Hurwitz stable by the nature of discretization, we can conclude that the dynamics of r given by (19) is stable. Furthermore, $L_1\alpha_1(h(z)A - L_1\alpha_1)^{-1}(h(z) - 1)(A\hat{C}_1 + BI)$ serves as an excitation term in (19), making r a function of z. That is, $z \neq 0 \implies h(z) \neq 1 \implies L_1\alpha_1(h(z)A - L_1\alpha_1)^{-1}(h(z) - 1)(A\hat{C}_1 + BI) \neq 0$, and this ultimately makes $r \neq 0$.

We can further see that under no crack, that is, z = 0 and h(z) = 1, we have

$$\dot{r} = Ar. \tag{20}$$

This indicates that $r \approx 0$.

3.2. Crack estimation filter

Crack estimation filter utilizes primary residual r as feedback signal. As shown in (19), r carries the signature of z. We denote the steady-state expression of this signature as r = g(z). Next, the crack estimation filter structure is given by

$$\dot{\hat{z}} = \beta_4 (A_{max} - \hat{z})|I| + L_2(r - g(\hat{z})), \tag{21}$$

where \hat{z} is the estimated crack and L_2 is the filter gain to be designed. Next proposition proves the convergence of the estimation.

Proposition 3. Consider the filter structure (21) and define the crack estimation error as $\tilde{z} = z - \hat{z}$. Furthermore, consider a linear approximation of the function $g(z) \approx \alpha_3 z + \alpha_4$, where α_3 and α_4 are linearization constants. Then, the error \tilde{z} remains bounded if the following condition is satisfied: $(-\beta_4|I|-L_2\alpha_3)<0$.

Proof. Subtracting (21) from (7), the error dynamics can be written as

$$\dot{\tilde{z}} = \dot{z} - \dot{\hat{z}} = -\beta_4 \tilde{z} |I| - L_2(g(z) - g(\hat{z})).$$
 (22)

Consider a linear approximation $g(z) \approx \alpha_3 z + \alpha_4$, where α_3 and α_4 are linearization constants. Under this linearized approximation, (23) becomes:

$$\dot{\tilde{z}} = (-\beta_4|I| - L_2\alpha_3)\tilde{z}. \tag{23}$$

If L_2 is chosen such that $(-\beta_4|I|-L_2\alpha_3)<0$, then the dynamics (23) is stable, and the error \tilde{z} will remain bounded and converge close to zero.

Remark 1. The observer gains L_1 and L_2 are designed according to the conditions given in Proposition 1 $((h(z)A - L_1\alpha_1)$ is Hurwitz stable $\forall z \in [0, A_{max}])$ and Proposition 3 $((-\beta_4|I|-L_2\alpha_3)<0)$, respectively. For numerically computing the observer gains, we discretized the sample space $[0, A_{max}]$ into 20 different points, and the gain L_1 was chosen to satisfy the condition at each of these points. Similarly, for proposition 3, we check the condition for some representative points within the sample space $[I_{min}, I_{max}]$, and chose the gain L_2 to satisfy these points.

4. Results and Discussion

In this section, we discuss the results from experimental and simulation studies performed to validate the proposed detection and identification framework.

First, we discuss the experiments performed to characterize the models discussed in Section 2. We used a commercial battery cell with the following properties: 4.2V to 2.5V operating voltages, with a capacity of 3500 mAh, anode and cathode which consists of a silicon-carbon composite and NMC811 ($LiNi_{0.8}Mn_{0.1}Co_{0.1}O_2$) composite respectively [26] [27]. The experiments were conducted with battery cells inside the ESPEC thermal chamber, connected to ARBIN battery testing equipment. The experimental schedules were created and fed into the ARBIN systems using the software MITS Pro.

An initial test of very low current (C/100 C-rate) was performed to obtain the open circuit voltage (OCV) characteristics of the cells. The OCVs as functions of state-of-charge are shown in Fig. 2.

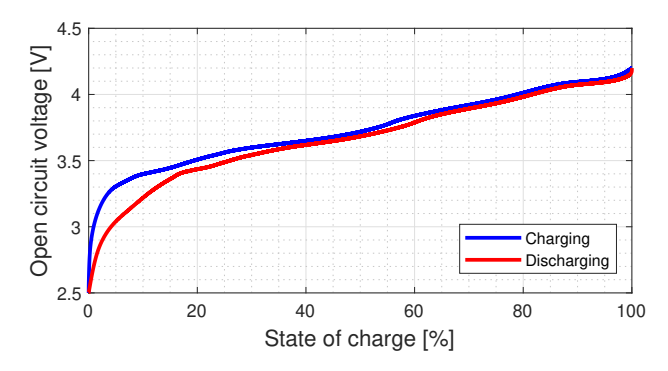


Figure 2: Open Circuit Potential maps for the battery cells.

Next, in order to differentiate the cracking from nominal no-crack scenarios, it is important to have relevant experimental datasets for both scenarios. To acquire such experimental data, we performed two controlled set of experiments as follows:

- 1. Nominal scenario: Battery cell # 1 was cycled at 25°C with (i) constant current constant voltage (CCCV) profile with 0.5C C-rate from 2.5V to 4.2V, and (ii) dynamic discharge current derived from a scaled-down Urban Dynamometer Discharge Schedule (UDDS), in order to emulate a real-world battery operation.
- 2. Cathode crack scenario: Battery cell # 2 was cycled at 25°C with (i) constant current constant voltage (CCCV) profile with 0.5C C-rate from 2.5V to 4.5V, and (ii) same dynamic discharge current as the nominal scenario.

Note that the only difference between nominal and cathode cracking scenarios above is the higher charge voltage limit. In the existing literature, it has been found that higher voltage limits can potentially induce cathode cracking [2] [11] [12]. The nominal cathode model and the crack model described in Section Section 2 are identified based on the first 30 cycles of these experimental data. The identified parameters are listed in Table 1. Furthermore, a comparison of the identified model voltage and experimental voltage

for 30 cycles are shown in Fig. 3. In Fig. 4 and 5, the voltage comparison are shown for cycle # 1 and cycle # 30, respectively. It has to be noted that the first cycle in Fig. 4 for both nominal scenario, as well as the cathode crack scenario, occurs after 12 hours of the experiments due to the presence of initial tests on the fresh cells.

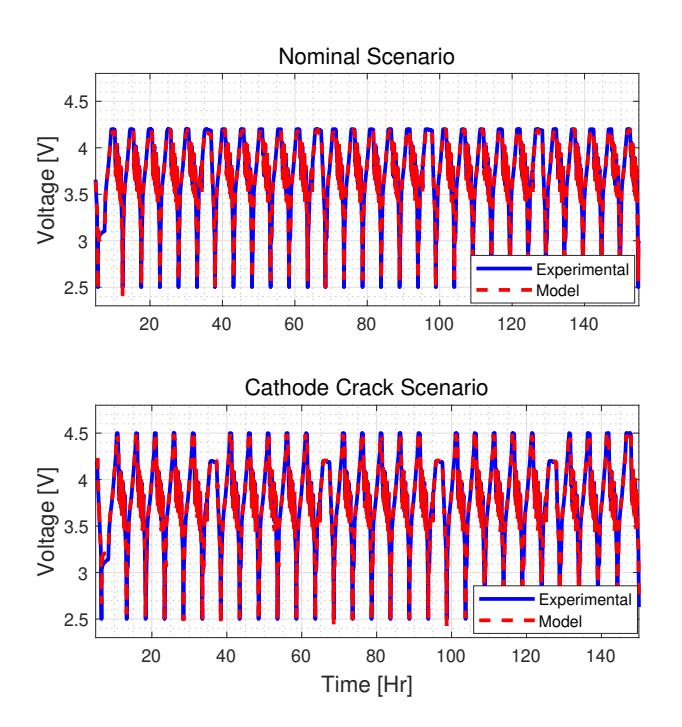


Figure 3: Comparison of experimental voltage and identified model voltage under nominal (no crack) and cathode crack scenarios. RMSE for nominal scenario is 0.031V, and RMSE for crack scenario is 0.037V.

Table 1: Cathode's identified model parameters

Notation	Description	Value [Units]
D_{s0}^+	Diffusion coefficient	$1 \times 10^{-14} \ [m^2/s]$
ϵ^+	Volume fraction	0.5938
A^+	Current collector area	$0.1324 \ [m^2]$
L^+	Thickness	$7 \times 10^{-5} \ [m]$
R^+	Radius	$8.21 \times 10^{-6} \ [m]$
C_{max}^+	Max conc. capacity	$5.139 \times 10^4 \ [mol/m^3]$

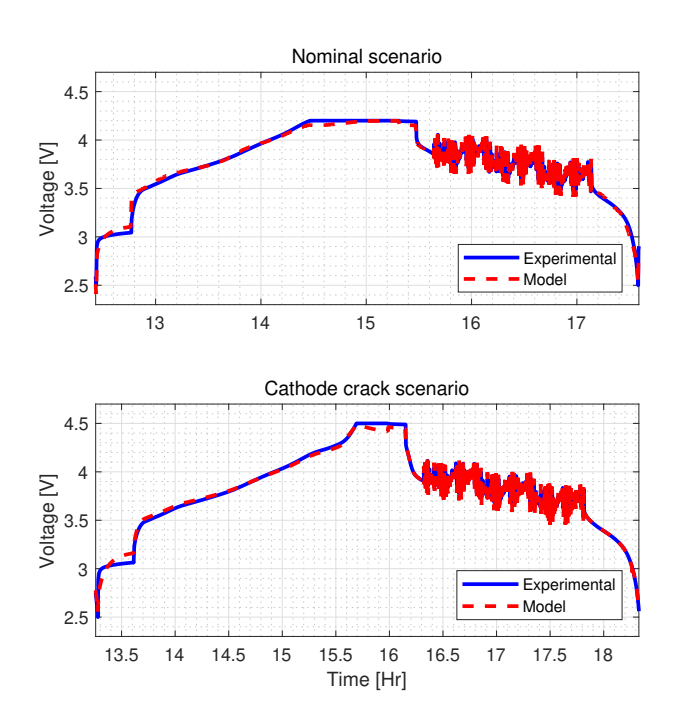


Figure 4: Comparison of experimental voltage and identified model voltage in cycle # 1 under nominal (no crack) and cathode crack scenarios.

Due to the charge/discharge cycling of the battery cells, the battery cells undergo nominal capacity loss even without cracking which is illustrated in Fig. 6. Due to the numerous electrochemical reactions that occur during the nominal operation of a battery cell, the battery tends to degrade resulting in a capacity fade. Two of the main reasons that lead to the battery cell degradation are the lithium plating of the negative electrode [28] and solid-electrode interface (SEI) layer growth [29]. On the other hand, the effect of the cathode crack manifested itself as higher levels of capacity loss (compared to the nominal scenario), as shown in Fig. 6. The nominal capacity loss (without the effect of cathode crack) was captured in the modeling framework by making the cathode volume fraction decrease over time. Under the nominal (no crack scenario) mentioned previously, this time-varying nature of the cathode volume fraction is shown in Fig. 7. Next, the additional capacity loss due to cathode crack manifested itself under cathode crack experiments. This crack effects are captured by the change in crack area A_{cr} , which in turn induces a change in the cathode diffusion coefficient,

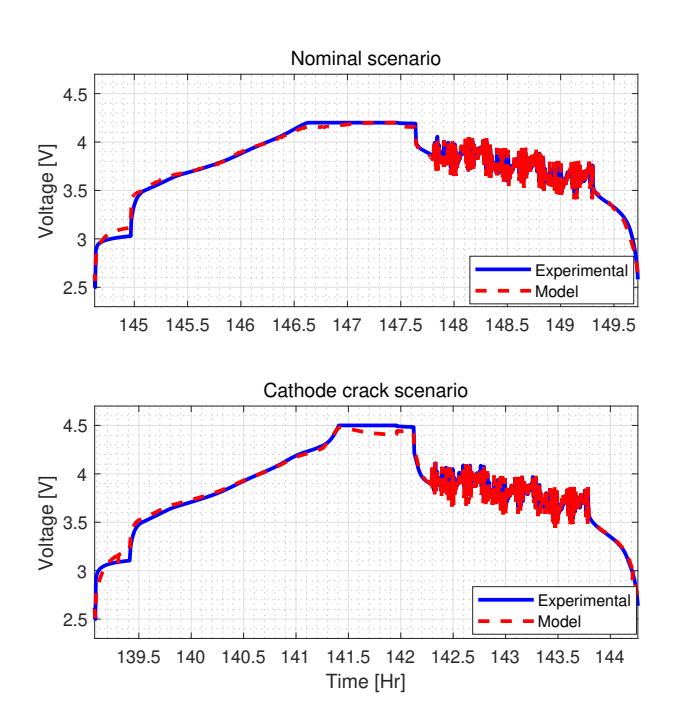


Figure 5: Comparison of experimental voltage and identified model voltage in cycle # 30 under nominal (no crack) and cathode crack scenarios.

as shown in Fig. 8. In summary: (i) the capacity loss under nominal (no crack) scenario is modelled by reducing the cathode volume fraction; and (ii) the capacity loss under cathode crack scenario is modelled by reducing the cathode volume fraction and increasing the crack area (which in turn reduces the cathode diffusion coefficient).

For no crack nominal scenario, we have accounted for the capacity fade by using reduction in the cathode volume fraction (loss of active material). However, when it comes to cathode crack scenario, the capacity fade occurs not only due to loss of active material but also due to crack growth. This crack growth results in the reduction of cathode's diffusion coefficient, as explained in [8]. To account for the capacity fade due to reduction in diffusion coefficient, we have adopted the modeling approach presented in [30]. As mentioned in [30], reduction in the diffusion coefficient accounts for the capacity loss due to rate capability. This rate capability loss occurs because of the transport limitations induced by the formation of oxide layers on the electrode. The solid phase diffusion coefficient is considered as the parameter

to account for such losses.

It has to be noted that in Fig. 6 the capacity fade due to crack from 1^{st} cycle to 30^{th} cycle is from 3.284 Ah to 3.079 Ah. Which is a reduction of around 6%. This is a significant reduction in the battery capacity which shows a great sign of aging - good enough for modeling purposes of the current work.

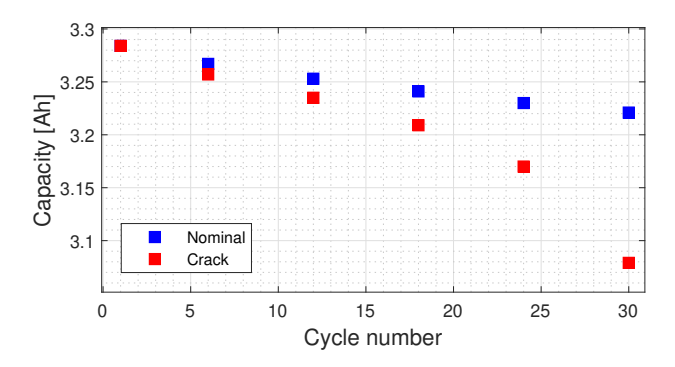


Figure 6: Comparison of the capacity fade in nominal case versus cathode crack case.

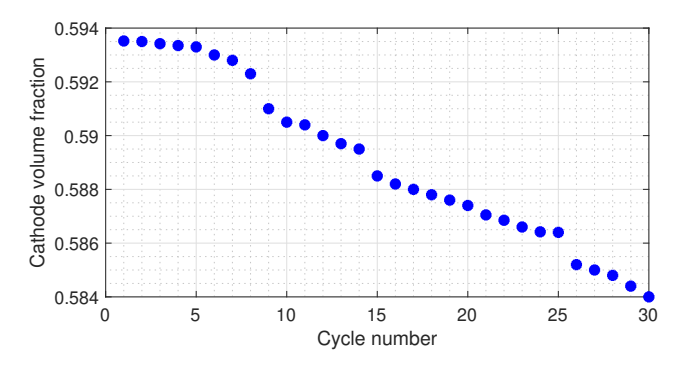


Figure 7: Evolution of cathode volume fraction with time due to nominal capacity loss.

Next, we discuss the performance of the proposed algorithm by using experimental data. That is, the experimental voltage and current data are fed to the algorithm as feedback signals. In turn, the algorithm detects and identifies the cathode crack area.

First, we evaluate the performance under cathode crack case, that is, using the date generated from cathode crack scenario in Section IV.A. As discussed in Section III, the voltage data is fed to the primary residual filter,

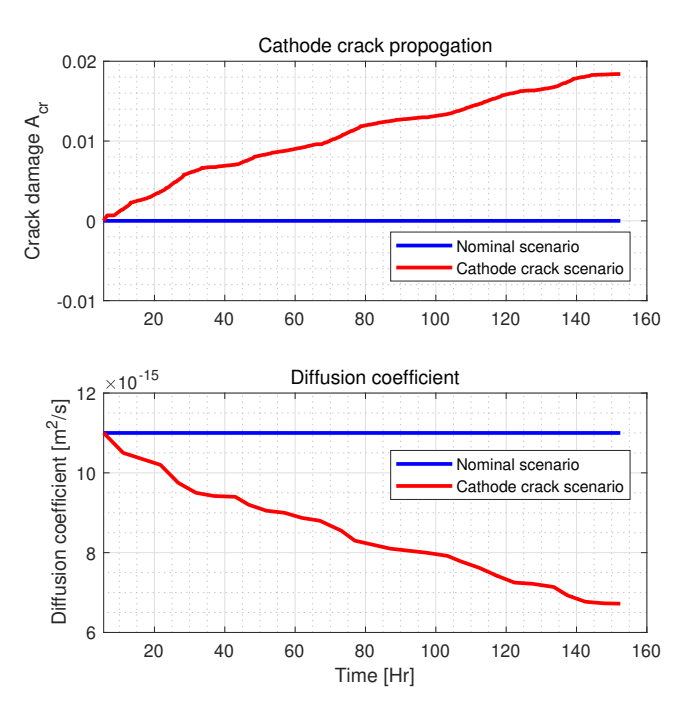


Figure 8: Crack area propagation and corresponding change in diffusion coefficient, under no crack and cathode crack scenarios.

which generates the primary residual signal, as shown in Fig. 9. As expected, the primary residual shows non-zero behavior, which arises from two components: propagation of cathode crack area and other unmodelled dynamics of cathode SPM. Next, we distinguish these two sources of errors. We see that the bottom envelope of the primary residual signal, denoted by the red * in Fig. 9, show a strong correlation with the crack area propagation plotted in the top plot of Fig. 8. The correlation between this bottom envelope and the crack area generated from the crack model is shown in Fig. 10. Next, we use this correlation to formulate the map g(z) discussed in Section III.B (just before (21)). The map takes the form of $g(z) = \gamma_1 z + \gamma_2(z)$ where γ_1 is a constant, and $\gamma_2(.)$ is a state-dependent parameter.

Subsequently, the crack estimation filter will use this map to generate an estimate of the crack area, as discussed in Section III.B. The crack estimation performance is shown in Fig. 11, where the offline identified crack area from the model and the online crack area estimate by the crack estimation filter are shown to have reasonable similarity - establishing the promise of the

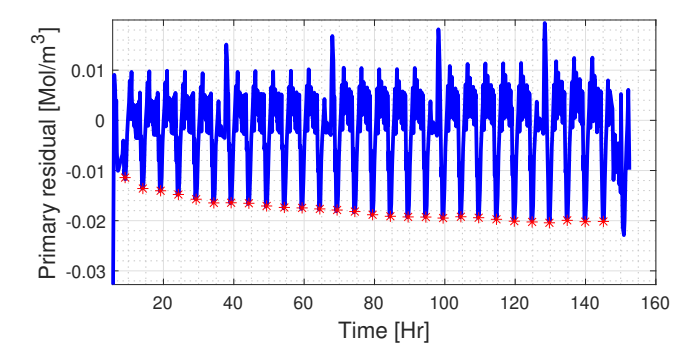


Figure 9: Primary residual signal under cathode crack scenario.

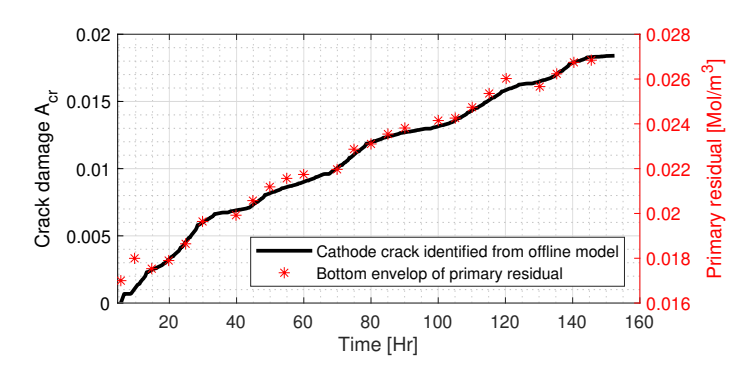


Figure 10: Correlating the primary residual envelope to the crack area propagation, under cathode crack scenario.

proposed algorithm.

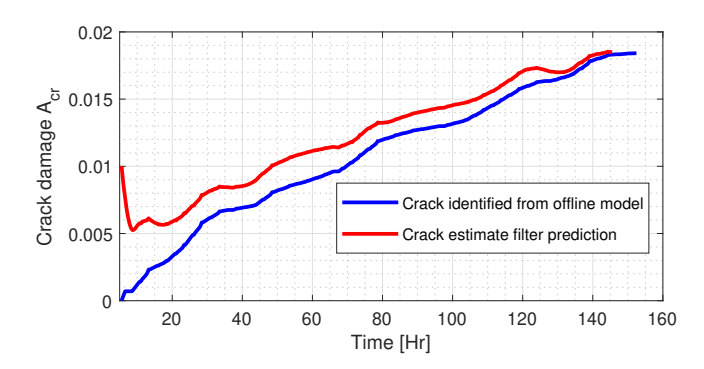


Figure 11: Performance of the crack estimation filter under cathode crack scenario. The average estimation error after convergence is 1.4×10^{-2} .

Next, we evaluate the performance under the no crack case, that is, using the data generated from the nominal (no crack) scenario in Section IV.A. As discussed in Section III, the voltage data is fed to the primary residual filter, which generates the primary residual signal, as shown in Fig. 12. The correlation between the bottom envelope of primary residual signal and the crack area generated from the crack model is shown in Fig. 13. Subsequently, based on this primary residual signal, the crack estimation performance is shown in Fig. 11, where the offline identified crack area from the model and the online crack area estimate by the crack estimation filter are shown to have reasonable similarity – establishing the promise of the proposed algorithm under no crack scenario. It is important to note that the map $g(z) = \gamma_1 z + \gamma_2(z)$ is tuned based on data from both cathode crack case and no crack case to ensure desired response from the crack estimation filter.

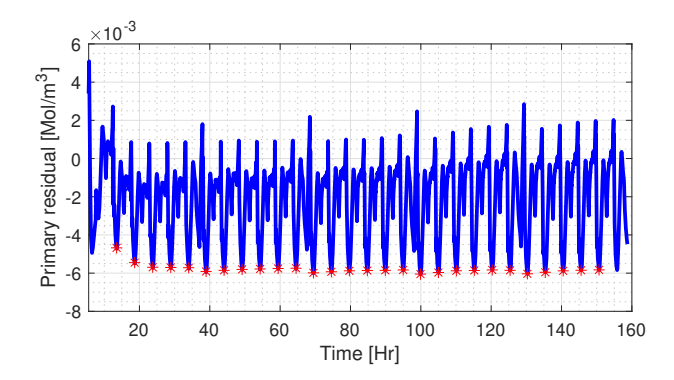


Figure 12: Primary residual signal under no crack (nominal) scenario.

Next, a few case studies are conducted to study the convergence properties of the proposed filters. First, we study the convergence of the primary residual filter. Three different initial conditions are given to the primary residual filter, as shown in Fig. 15. As can be seen, the residual signal converged in all the three cases – illustrating the filter's ability to converge from arbitrary incorrect initial conditions. The convergence of the crack estimation filter under these three initial conditions of primary residual filter is shown in Fig. 16, which confirms that the crack estimation filter's performance remain almost unaffected by these arbitrary incorrect initial conditions.

Next, we study the convergence properties of crack estimation filter when it is initialized with different incorrect conditions. Three different initial conditions are given to the crack estimation filter, for all of which the crack

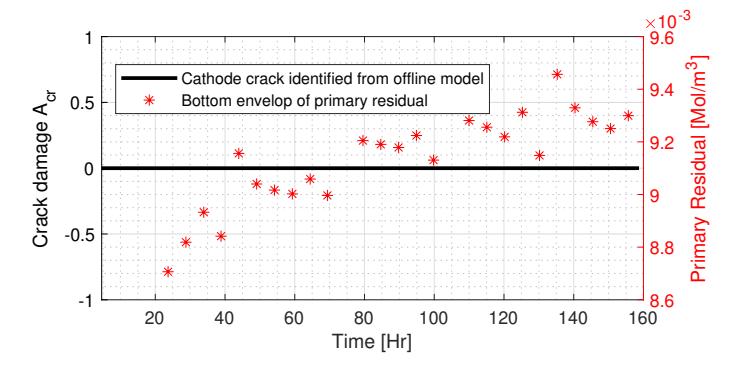


Figure 13: Correlating the primary residual envelope to the crack area propagation, under no crack (nominal) scenario.

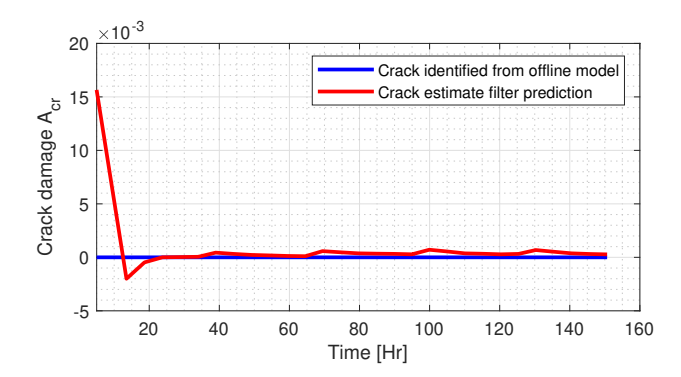


Figure 14: Performance of the crack estimation filter under no crack (nominal) scenario. The average estimation error after convergence is 3.69×10^{-4} .

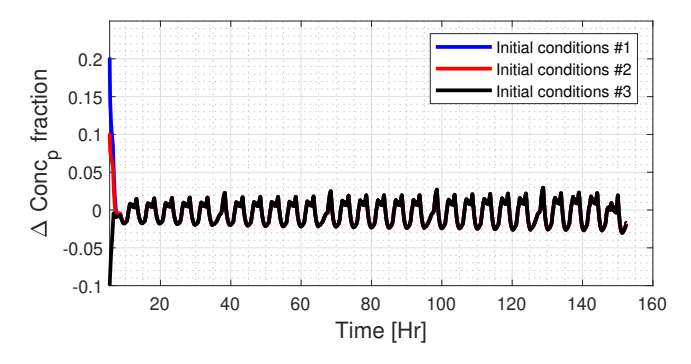


Figure 15: Convergence study of the primary residual filter, under different primary residual initial conditions.

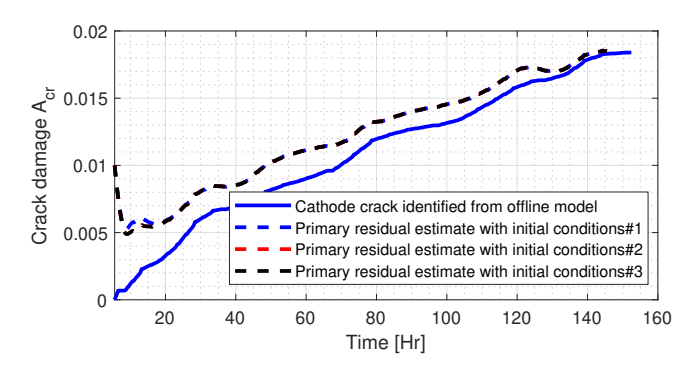


Figure 16: Convergence of the crack estimation, under different primary residual initial conditions.

estimate converged to similar values, as shown in Fig. 17. This verifies that the crack estimation filter also possesses reasonable convergence properties.

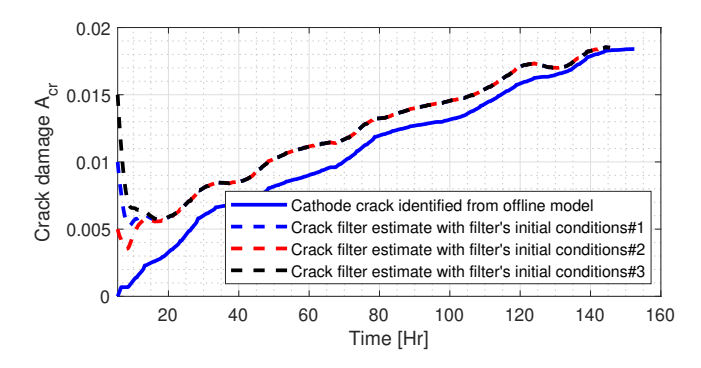


Figure 17: Convergence study of crack estimation filter, under different crack estimation initial conditions.

Next, we summarize the findings of our results. First, we have gathered experimental data from commercial battery cells capturing two scenarios: nominal (no crack) and cathode crack scenario. Inspired by experimental studies in existing literature, cathode crack was induced by overcharging a battery cell to a higher cut-off voltage. Next, coupled SPM and cathode crack models are identified based on these two datasets. Subsequently, these identified models are used to design primary residual filter. Then, the primary residual signal was correlated with the identified crack propagation. This correlation was used to create a mapping from primary residual signal to a nonlinear crack feedback signal. Next, this nonlinear map and crack

model are used to design crack estimation filter, which estimates the crack propagation. The efficacy of the proposed algorithm was tested using experimental data. The convergence properties of primary residual filter and crack estimation filter are tested by giving various incorrect initial conditions.

5. Conclusion

This work utilizes a coupled dynamical model consisting of modified electrochemical SPM and cathode crack model. Based on this model, an algorithmic framework consisting of two filters is designed. The first filter is the primary residual filter which generates a primary residual signal using cathode SPM and voltage feedback. The primary residual signal is essentially the difference between closed-loop and open-loop estimates of cathode concentration. This primary residual signal is used by the second filter, denoted as the crack estimation filter. The crack estimation filter uses primary residual signal as feedback, and in turn, estimates the crack propagation. First, we have gathered experimental data from commercial battery cells capturing two scenarios: nominal (no crack) and cathode crack scenario. Nominal capacity fade was captured by the reduction in cathode active material volume fraction. The additional capacity fade due to the crack was captured by by reduction in the effective cathode diffusion coefficient. These two datasets are used to test the effectiveness of the proposed algorithm, which shows reasonable performance. It has to be noted that the current work is validated on only one particular battery chemistry over a limited number of operational cycles. Further study is required to validate the algorithm's effectiveness under different cell chemistries and longer operational cycles. As a future extension of this work, we plan to address these along with extending the experimental studies to capture longer-term behavior under cathode cracks.

Acknowledgement

This work was supported by National Science Foundation under Grant No. 2050315. The opinions, findings, and conclusions or recommendations expressed are those of the author(s) and do not necessarily reflect the views of the National Science Foundation.

References

- [1] S. Pelletier, O. Jabali, G. Laporte, M. Veneroni, Battery degradation and behaviour for electric vehicles: Review and numerical analyses of several models, Transportation Research Part B: Methodological 103 (2017) 158–187.
- [2] P. Li, Y. Zhao, Y. Shen, S.-H. Bo, Fracture behavior in battery materials, Journal of Physics: Energy 2 (2020) 022002.
- [3] R. Deshpande, M. Verbrugge, Y.-T. Cheng, J. Wang, P. Liu, Battery cycle life prediction with coupled chemical degradation and fatigue mechanics, Journal of the Electrochemical Society 159 (2012) A1730.
- [4] I. Laresgoiti, S. Käbitz, M. Ecker, D. U. Sauer, Modeling mechanical degradation in lithium ion batteries during cycling: Solid electrolyte interphase fracture, Journal of Power Sources 300 (2015) 112–122.
- [5] J. Wang, J. Purewal, P. Liu, J. Hicks-Garner, S. Soukazian, E. Sherman, A. Sorenson, L. Vu, H. Tataria, M. W. Verbrugge, Degradation of lithium ion batteries employing graphite negatives and nickel—cobalt—manganese oxide+ spinel manganese oxide positives: Part 1, aging mechanisms and life estimation, Journal of Power Sources 269 (2014) 937–948.
- [6] X. Li, A. M. Colclasure, D. P. Finegan, D. Ren, Y. Shi, X. Feng, L. Cao, Y. Yang, K. Smith, Degradation mechanisms of high capacity 18650 cells containing si-graphite anode and nickel-rich nmc cathode, Electrochimica Acta 297 (2019) 1109–1120.
- [7] J. M. Reniers, G. Mulder, D. A. Howey, Review and performance comparison of mechanical-chemical degradation models for lithium-ion batteries, Journal of The Electrochemical Society 166 (2019) A3189–A3200.
- [8] P. Barai, K. Smith, C.-F. Chen, G.-H. Kim, P. P. Mukherjee, Reduced order modeling of mechanical degradation induced performance decay in lithium-ion battery porous electrodes, Journal of The Electrochemical Society 162 (2015) A1751.
- [9] J. Li, K. Adewuyi, N. Lotfi, R. G. Landers, J. Park, A single particle model with chemical/mechanical degradation physics for lithium

- ion battery state of health (soh) estimation, Applied energy 212 (2018) 1178–1190.
- [10] G. Dong, J. Wei, A physics-based aging model for lithium-ion battery with coupled chemical/mechanical degradation mechanisms, Electrochimica Acta 395 (2021) 139133.
- [11] P. Yan, J. Zheng, M. Gu, J. Xiao, J.-G. Zhang, C.-M. Wang, Intragranular cracking as a critical barrier for high-voltage usage of layer-structured cathode for lithium-ion batteries, Nature communications 8 (2017) 14101.
- [12] R. Xu, Theories and Experiments on the Electro-Chemo-Mechanics of Battery Materials (2019).
- [13] X.-D. Zhang, F.-S. Yue, J.-Y. Liang, J.-L. Shi, H. Li, Y.-G. Guo, Structure design of cathode electrodes for solid-state batteries: challenges and progress, Small Structures 1 (2020) 2000042.
- [14] J.-M. Lim, T. Hwang, D. Kim, M.-S. Park, K. Cho, M. Cho, Intrinsic origins of crack generation in ni-rich lini0. 8co0. 1mn0. 1o2 layered oxide cathode material, Scientific reports 7 (2017) 39669.
- [15] L. G. Bland, J. S. Locke, Chemical and electrochemical conditions within stress corrosion and corrosion fatigue cracks, npj Materials Degradation 1 (2017) 12.
- [16] R. Xu, H. Sun, L. S. de Vasconcelos, K. Zhao, Mechanical and structural degradation of linixmnycozo2 cathode in li-ion batteries: an experimental study, Journal of The Electrochemical Society 164 (2017) A3333.
- [17] D. Zhang, S. Dey, L. D. Couto, S. J. Moura, Battery adaptive observer for a single-particle model with intercalation-induced stress, IEEE Transactions on Control Systems Technology 28 (2020) 1363–1377. doi:10.1109/TCST.2019.2910797.
- [18] S. Santhanagopalan, Q. Guo, P. Ramadass, R. E. White, Review of models for predicting the cycling performance of lithium ion batteries, Journal of power sources 156 (2006) 620–628.

- [19] S. Sattarzadeh, S. Dey, A. Colclasure, K. Smith, Addressing the observability problem in batteries: Algorithm design for electrode-level charge and health estimation, in: 2020 American Control Conference (ACC), IEEE, 2020, pp. 1131–1136.
- [20] S. Dey, Y. Shi, K. Smith, A. M. Colclasure, X. Li, From battery cell to electrodes: Real-time estimation of charge and health of individual battery electrodes, IEEE Transactions on Industrial Electronics 67 (2019) 2167–2175.
- [21] R. Firoozi, S. Sattarzadeh, S. Dey, Cylindrical battery fault detection under extreme fast charging: A physics-based learning approach, IEEE Transactions on Energy Conversion 37 (2021) 1241–1250.
- [22] S. K. Padisala, S. Sattarzadeh, S. Dey, Reduced and reformulated electrochemical model-based detection and isolation of electrode-level faults in lithium-ion battery cells, IFAC-PapersOnLine 55 (2022) 734-739. URL: https://www.sciencedirect.com/science/article/pii/S2405896322029123. doi:https://doi.org/10.1016/j.ifacol.2022.11.269, 2nd Modeling, Estimation and Control Conference MECC 2022.
- [23] C. D. Rahn, C.-Y. Wang, Battery systems engineering, John Wiley & Sons, 2013.
- [24] S. J. Moura, N. A. Chaturvedi, M. Krstic, Pde estimation techniques for advanced battery management systems—part i: Soc estimation, in: 2012 American Control Conference (ACC), IEEE, 2012, pp. 559–565.
- [25] D. Di Domenico, A. Stefanopoulou, G. Fiengo, Lithium-ion battery state of charge and critical surface charge estimation using an electrochemical model-based extended kalman filter, Journal of dynamic systems, measurement, and control 132 (2010).
- [26] X. Li, A. M. Colclasure, D. P. Finegan, D. Ren, Y. Shi, X. Feng, L. Cao, Y. Yang, K. Smith, Degradation mechanisms of high capacity 18650 cells containing si-graphite anode and nickel-rich nmc cathode, Electrochimica Acta 297 (2019) 1109-1120. URL: https://www.sciencedirect.com/science/article/pii/S0013468618326781. doi:https://doi.org/10.1016/j.electacta.2018.11.194.

- [27] T. M. Heenan, A. Jnawali, M. Kok, T. G. Tranter, C. Tan, A. Dimitrijevic, R. Jervis, D. Brett, P. Shearing, An advanced microstructural and electrochemical datasheet on 18650 li-ion batteries with nickel-rich nmc811 cathodes and graphite-silicon anodes, Journal of The Electrochemical Society 167 (2020) 140530.
- [28] E. Redondo-Iglesias, P. Venet, S. Pelissier, Calendar and cycling ageing combination of batteries in electric vehicles, Microelectronics Reliability 88-90 (2018) 1212-1215. URL: https://www.sciencedirect.com/science/article/pii/S0026271418305377. doi:https://doi.org/10.1016/j.microrel.2018.06.113, 29th European Symposium on Reliability of Electron Devices, Failure Physics and Analysis (ESREF 2018).
- [29] Y. Zeng, F. Shen, B. Zhang, J. Lee, D. Chalise, Q. Zheng, Y. Fu, S. Kaur, S. D. Lubner, V. S. Battaglia, et al., Nonintrusive thermal-wave sensor for operando quantification of degradation in commercial batteries, Nature Communications 14 (2023) 8203.
- [30] P. Ramadass, B. Haran, R. White, B. N. Popov, Mathematical modeling of the capacity fade of li-ion cells, Journal of power sources 123 (2003) 230–240.